Comparison of low-molecular-weight ligand and whole antibody in prostate-specific membrane antigen targeted near-infrared photoimmunotherapy

Kohei Nakajima†, Fuka Miyazaki†, Kazuki Terada, Hideo Takakura, Motofumi Suzuki, Mikako Ogawa*

Laboratory of Bioanalysis and Molecular Imaging, Graduate School of Pharmaceutical Sciences, Hokkaido University, Sapporo, Hokkaido, Japan

†These authors contributed equally to this work.

*Corresponding author: Mikako Ogawa

Laboratory of Bioanalysis and Molecular Imaging, Graduate School of Pharmaceutical Sciences, Hokkaido University, Sapporo, Hokkaido 060-0812, Japan

Phone: +81-11-706-3767, Fax: +81-11-706-3767.

E-mail: mogawa@pharm.hokudai.ac.jp

Abstract

Near-infrared photoimmunotherapy (NIR-PIT) is a cancer phototherapy that uses antibody-IR700 conjugate (Ab-IR700) and NIR light. Ab-IR700 forms aggregates on the plasma membranes of targeted cancer cells after light exposure, inducing lethal physical damage within the membrane. Low-molecular-weight (LMW) ligands are candidate targeting moieties instead of antibodies, but whether LMW-IR700 conjugates induce cell death by aggregation, the same mechanism as Ab-IR700, is unknown. Thus, we investigated differences in cytotoxicity and mechanisms between LMW-IR700 and Ab-IR700 targeting prostate-specific membrane antigen (PSMA). Both conjugates decreased cell viability to the same degree after light irradiation, but different morphological changes were observed in PSMA-positive LNCaP cells by microscopy. Cell swelling and bleb formation were induced by Ab-IR700, but only swelling was observed in cells treated with LMW-IR700, suggesting the cells were damaged via different cytotoxic mechanisms. However, LMW-IR700 induced bleb formation, a hallmark of NIR-PIT with Ab-IR700, when singlet oxygen was quenched or LMW-IR700 was localized only on the plasma membrane. Moreover, the water-soluble axial ligands of LMW-IR700 were cleaved, consistent with previous reports on Ab-IR700. Thus, the main cytotoxic mechanisms of Ab-IR700 and LMW-IR700 differ, although

LMW-IR700 on the plasma membrane can cause aggregation-mediated cytotoxicity as well as Ab-IR700.

Keywords: Low-molecular-weight ligand, Molecular targeted therapy, Near-infrared photoimmunotherapy (NIR-PIT), Photodynamic therapy (PDT), Photosensitizer

1. Introduction

Near-infrared photoimmunotherapy (NIR-PIT) is a newly developed molecular-targeted cancer therapy with an antibody-photosensitizer conjugate, which utilizes photosensitive IRDye700DX (IR700) (Mitsunaga et al., 2011)(Kobayashi and Choyke, 2019). Immunogenic cell death is rapidly induced when the antibody-IR700 conjugate (Ab-IR700) binds to an antigen of cancer cells and is exposed to NIR light. Furthermore, NIR-PIT against various targeted antigens on cells was effective in mouse models (Nagaya et al., 2016)(Nagaya et al., 2017a)(Nishimura et al., 2019)(Mao et al., 2018), and a worldwide Phase III clinical trial of NIR-PIT in patients with inoperable head and neck cancer is currently running (https://clinicaltrials.gov/ct2/show/NCT03769506). In September 2020, the Ministry of Health, Labour and Welfare of Japan approved NIR-PIT using a Cetuximab-IR700 conjugate that targets the epidermal growth factor receptor (EGFR).

Most NIR-PIT agents, including clinically approved drugs, utilize antibodies as a targeting moiety. However, low-molecular-weight (LMW) ligands have several advantages including faster pharmacokinetics and a lower cost of manufacturing (Henninot et al., 2018)(Morales-Cruz et al., 2019) and they have been used to deliver IR700 to cancer cells as an alternative to antibodies (Wang et al., 2016)(Chen et al.,

2017). Wang et al. reported LMW ligands-IR700 conjugates (LMW-IR700) targeted prostate specific membrane antigen (PSMA), which is specifically expressed by malignant prostate tumor cells (Wang et al., 2016). The administered conjugates rapidly accumulated in PSMA-positive target tumors and promoted *in vivo* therapeutic outcomes after light irradiation. That study also reported that reactive oxygen species (ROS) generated by LMW-IR700 killed cancer cells after NIR light exposure, a known mechanism of photodynamic therapy (PDT) (Dolmans et al., 2003)(Yoo and Ha, 2012).

Light-irradiated IR700 was reported to induce the production of ROS (Wei et al., 2019) and IR700 is a highly unique photoreactive molecule that forms water-insoluble aggregation via photochemical reactions (Sato et al., 2018)(Kobayashi et al., 2020). During this aggregating process, IR700 changes its properties from hydrophilic to hydrophobic by releasing water-soluble axial ligands triggered by NIR light, and the aggregation of Ab-IR700 induces lethal physical damage within the plasma membranes of target cells. Given the cytotoxic mechanism of Ab-IR700 in NIR-PIT, LMW-IR700 might also cause cellular damage via aggregation, a mechanism different from that of PDT. However, previous reports of LMW-IR700 did not focus on its unique cytotoxic mechanism (Wang et al., 2016)(Chen et al., 2017)(Dou et al., 2018).

Thus, the purpose of this study was to elucidate the mechanisms of cytotoxicity

induced by LMW-IR700 after NIR light irradiation. In this paper, we synthesized an LMW-IR700 conjugate that binds to PSMA-positive cancer cells. Using this conjugate, we investigated potential differences in cytotoxicity and mechanisms between LMW-IR700 and Ab-IR700. To elucidate the unknown cytotoxic mechanisms of LMW-IR700 is important for developing new drugs in NIR-PIT using targeting molecules (e.g., small organic ligands, peptides, aptamers) as alternatives to antibodies.

2. Materials and methods

2.1. Reagents

Anti-PSMA monoclonal antibody (Clone: YPSMA-1) was purchased from Abcam (Cambridge, UK). Water-soluble, silicon-phthalocyanine derivative, IRDye700DX NHS ester was obtained from Li-COR Bioscience (Lincoln, NE, USA). All other chemicals were of reagent grade.

2.2. Synthesis of LMW-IR700

An LMW ligand composed of Glu-Urea-Lys was synthesized in two steps according to a previous study (Choy and Berkman, 2016). Carbonyldiimidazole (0.20 g, 1.6 mmol) was added to a solution of H-Glu(OBzl)-OBzl·Tos-OH (0.18 g, 0.50 mmol) and Et_3N (0.069 mL, 0.050 mmol) in 5 mL of anhydrous dichloromethane (DCM), and the reaction mixture was stirred under an Argon atmosphere for 17 h at room temperature. Then, H-Lys(Z)-OBzl·HCl (0.51 g, 1.2 mmol) and Et_3N (0.17 mL, 1.2 mmol) in 3 mL of anhydrous DCM were added to the reaction mixture dropwise and stirred until completion. The reaction mixture was concentrated and the crude mixture was dissolved in DCM (20 mL) and washed with saturated NH_4Cl (2X, 20 mL), followed by water then brine. The organic layer was dried over Na_2SO_4, filtered, and

evaporated. The product was purified by silica-gel column chromatography (EtOAc:Hexane = 2:3 as the eluent) to generate a white solid (46.8 mg, 13% yield). ^{1}H NMR (400 MHz, DMSO-d_6): δ 7.35-7.20 (m, 20H), 6.49 (d, J = 8.5 Hz, 1H), 6.45 (d, J = 8.1 Hz, 1H), 5.11-4.96 (m, 8H), 4.24-4.18 (m, 1H), 4.13-4.08 (m, 1H), 2.90 (q, J = 6.3 Hz, 2H), 2.43-2.33 (m, 2H), 2.01-1.92 (m, 1H), 1.83-1.73 (m, 1H), 1.66-1.47 (m, 2H), 1.36 (m, 2H), 1.21 (m, 2H).

Pd/C (5.8 mg) was added to a solution of the product (30 mg, 0.036 mmol) in 2 mL of MeOH/DCM (1:1) under an H_2 atmosphere and the reaction mixture was stirred for 7 h at room temperature. Then, the Pd/C was filtered off and the filtrate was evaporated. The product (LMW ligand) was obtained as a white solid (10.8 mg, 94% yield). HRMS (ESI$^+$): *m/z* calcd. for $C_{12}H_{22}N_3O_7^+$: 320.15 $[M+H]^+$; found: 320.09.

The LMW ligand (0.75 mg, 2.34 μmol) was added to the IR700 NHS ester (0.48 mg, 0.25 μmol) and *i*Pr$_2$EtN (0.032 mg, 0.25 μmol) in 350 μL of DMSO. The reaction mixture was stirred under an Argon atmosphere at 40°C for 19 h. The crude product was purified by semipreparative reverse phase high-performance liquid chromatography (HPLC), using eluent A (H_2O, 0.1 M triethylammonium acetate (TEAA)) and eluent B (99% MeCN, 1% H2O) (A/B = 70/30 in 15 min, 70/30 to 0/100 in 5 min). The product was desalted with a Sep-Pak C18 cartridge (Waters Corporation, Milford, MA, USA)

and obtained as a blue solid (0.35 mg, 64% yield). HRMS (ESI): *m/z* calcd. for $C_{82}H_{111}N_{14}Na_4O_{31}S_6Si_3^{2-}$: 1077.74 $[M-2H]^{2-}$; found: 1077.23.

2.3. Synthesis of Ab-IR700

Anti-PSMA antibody (0.50 mg, 3.4 nmol) was incubated with the IR700 NHS ester (0.022 mg, 12 nmol) in 0.1 M Na_2HPO_4 (pH 8.5) at room temperature for 3 h. The mixture was purified with a Sephadex G25 column (PD-10; GE Healthcare, Milwaukee, WI, USA). The protein concentration was determined with a Pierce™ Modified Lowry Protein Assay Kit (Thermo Fisher Scientific Inc., Rockford, IL, USA) by measuring the absorption at 750 nm using a microplate reader (Infinite M200 instrument, Tecan Austria GmbH, Grödig, Austria). The concentration of IR700 was measured by absorption at 689 nm to confirm the number of dyes per antibody. The synthesis was controlled so that a mean of three IR700 molecules were bound to a single antibody.

2.4. Cell culture

Two human prostate carcinoma cell lines were purchased from American Type Culture Collection (ATCC, Manassas, VA, USA): LNCaP (PSMA-positive) and DU145 (PSMA-negative). The cells were cultured in RPMI 1640 medium (Sigma, St Louis,

MO, USA) supplemented with 10% fetal bovine serum (Gibco Life Technologies, Grand Island, NY, USA) and 1% penicillin/streptomycin (Nacalai Tesque, Kyoto, Japan) in a humidified incubator at 37°C and 5% CO_2.

2.5. Fluorescence microscopy

To detect the antigen-specific binding and uptake of LMW-IR700, fluorescence imaging was performed using a fluorescence microscope (BX41 microscope, Olympus Corporation, Tokyo, Japan). LNCaP or DU145 cells were plated on coverslips and 48 h later, cells were incubated with LMW-IR700 for 1 h at 37°C (final concentration of IR700: 0.1 μM). After cells were washed with phosphate buffered saline (PBS), IR700 fluorescence was observed using a fluorescence microscope (BX41 microscope, Olympus Corporation), which has a 670–745 nm excitation filter and a 769–849 nm emission filter.

To investigate the subcellular localization of LMW-IR700 and Ab-IR700, LNCaP cells were seeded in 35-mm glass-bottom culture dishes. Each conjugate was added to the culture medium (final concentration of IR700: 0.1 μM) and incubated for 1 h at 37°C. Lysosomes were stained with LysoTracker® Green DND-26 (Thermo Fisher Scientific Inc.). Before microscopic imaging, medium containing IR700 conjugates was

washed out and replaced with flesh phenol-red-free RPMI 1640 medium. Images of LysoTracker® Green and IR700 fluorescence were obtained using a confocal fluorescence microscope with a 100 × objective lens (Nikon A1, Nikon Co. Ltd., Tokyo, Japan). To detect the fluorescence of LysoTracker® Green, a 488-nm blue laser and a 500–550 nm band-pass emission filter were used. To detect the fluorescence of IR700, a 638-nm red laser and a 662–737 nm emission filter were used.

Image analysis was carried out with ImageJ 1.49v software (http://rsb.info.nih.gov/ij/).

2.6. NIR-PIT with LMW-IR700 and Ab-IR700

To compare the cytotoxicity induced by LMW-IR700 and Ab-IR700, microscopic observations were performed using a fluorescence microscope (CKX41, Olympus Corporation). First, 1.5×10^6 LNCaP cells were seeded on dishes and incubated for 48 h at 37°C. Then, the cells were irradiated with NIR light through the excitation filter of the microscope (673–748 nm) after the following treatments.

The dead cells induced by LMW-IR700 and Ab-IR700 were observed with propidium iodide (PI; Sigma), which detects compromised plasma membranes. LMW-IR700 or Ab-IR700 was added to the culture medium and incubated for 1 h at 37°C

(final concentration of IR700: 0.1 μM). PI was added to the medium at 30 min prior to NIR light exposure (1, 3, or 5 min).

To investigate the contribution of the enzyme reactions to cytotoxicity, microscopic observations were performed under a low temperature of 4°C. Cells were incubated with LMW-IR700 or Ab-IR700 for 1 h at 37°C. After the medium was replaced with cold medium, cells were irradiated with NIR light for 5 min at 4°C.

To examine the role of singlet oxygen ($^1O_2$) in LMW-IR700 or Ab-IR700-mediated phototoxicity, sodium azide (NaN_3) as an $^1O_2$ quencher was added to the medium at 5 min prior to NIR light exposure. The final concentration of NaN_3 was adjusted to 0, 1, or 10 mM. In this experiment, the incubation time with LMW-IR700 or Ab-IR700 was 1 h and the irradiation time of NIR light was 5 min.

To assess the cytotoxic effects induced by LMW-IR700 or Ab-IR700 bound to plasma membranes, cells were exposed to light under conditions where the agents were localized only on the membrane. Cells were incubated with LMW-IR700 or Ab-IR700 for 5 min at 4°C to inhibit their internalization via endocytosis, and then the medium was replaced with cold medium. Cells were irradiated with NIR light at 4°C for 5 min. All Image analyses were conducted using ImageJ 1.49v software.

2.7. Cell viability assay

To quantitatively evaluate the cytotoxicity induced by LMW-IR700 and Ab-IR700, cell viability was assessed using an MTT assay. Briefly, LNCaP cells were seeded in 48-well plates at a density of 20,000 cells per well. After 48 h incubation, LMW-IR700 or Ab-IR700 were added to the culture medium (final concentration of IR700: 0.1 μM) and incubated for 1 h at 37°C. Then, cells were irradiated by a laser emitting light at a 690 nm wavelength (MLL-III-690-800mW, Changchun New Industries Optoelectronics Technology Co., Ltd., Changchun, China) and at a power density of 50 mW/cm^2 as measured with an optical power meter (PM 100, Thorlabs, Newton, NJ, USA). At 24 h after NIR light exposure, MTT (Dojindo Laboratories, Kumamoto, Japan) solution was added and incubated for 45 min at 37°C. The medium was replaced with 200 μL of DMSO to dissolve the formazan crystals formed by living cells. The absorbance was measured at 535 nm with a microplate reader (Infinite M200 instrument).

2.7. Photoinduced ligand release of LMW-IR700

A 1.5 mL sample of 2.5 mM LMW-IR700 in PBS containing 0, 1, or 5 mM L-cysteine as an electron donor was prepared in a glass vial. Then, samples that had been

irradiated with NIR light (2 or 10 J/cm^2) or irradiated after bubbling argon through the septum cap of a sealed vial for 20 min, were analyzed by HPLC (Shimadzu Co., Kyoto, Japan) with a reverse-phase column Inertsil ODS-3 (10 mm × 250 mm) (GL Sciences Inc., Tokyo, Japan). The mobile phase consisted of 0.1 M TEAA in H_2O (A) and 99% acetonitrile, 1% H_2O (B), delivered at a flow rate of 1 mL min^{-1}. The gradient condition was set as 30% B (15.0 min), 40% to 100% B (15.1−20.0 min), and STOP (25 min). Then, 10 μL of each sample was mixed with 10 μL of 10 μM methylene blue as an internal standard, and 10 μL of the mixture was injected. A calibration curve to quantify the change in concentration of LMW-IR700 before and after irradiation was prepared by plotting the peak area ratio vs the concentration ratio of LMW-IR700 to methylene blue.

Two degradation products obtained by photolysis were isolated and characterized by MS. LMW-IR700-1; HRMS (ESI): *m/z* calcd. for $C_{68}H_{83}N_{13}O_{22}S_3Si_2^{2-}$: 792.7243 [M-2H]$^{2-}$; found: 792.7261. LMW-IR700-2; HRMS (ESI): *m/z* calcd. for $C_{54}H_{53}N_{12}O_{13}Si^-$: 1105.3630 [M]$^-$; found: 1105.3665.

2.8. Statistical analysis

Data are expressed as the means ± standard error of the mean (SEM) from a

minimum of three experiments. Statistical analyses were carried out using JMP Pro 14.0.0 software (SAS Institute Inc., Cary, NC, USA). Differences in mean values were assessed using the Student's *t*-test. A *p*-value less than 0.05 was considered statistically significant.

3. Results

3.1. LMW-IR700 specifically binds to PSMA-positive cells and induces cell death after NIR light irradiation.

The synthetic scheme of LMW-IR700 is shown in Fig. 1A. The conjugation of IR700 with LMW ligand and antibody was confirmed with UV-Vis-NIR spectroscopy (Fig. S1). First, we investigated the specific uptake and cytotoxicity of the synthesized LMW-IR700 (Fig. 2A). IR700 fluorescence was observed in PSMA-positive LNCaP, indicating the uptake of LMW-IR700. In contrast, IR700 fluorescence was not detected in PSMA-negative DU145. These results suggested that LMW-IR700 specifically bound to PSMA-positive cells. Fig. 2B shows the microscopic images of LNCaP treated with or without LMW-IR700 and NIR light exposure. In cells treated with both LMW-IR700 addition and NIR light irradiation, cell death accompanied by cell swelling was observed post irradiation (lower right). In contrast, other control cells, which were not treated with either LMW-IR700 addition or light irradiation, were not damaged.

3.2. Different morphological changes are induced in cells treated with LMW-IR700 or Ab-IR700.

To compare differences in cytotoxicity induced by LMW-IR700 and Ab-IR700, we obtained Ab-IR700 targeting PSMA in the procedure shown in Fig. 1B. Fig. 3A shows the morphological changes of cells treated with LMW-IR700 (top) or Ab-IR700 (bottom). Magnified microscopic images of cells before and 30 min after light irradiation are also shown. In cells treated with LMW-IR700, swelling was observed immediately after NIR light irradiation (5 min). At 30 min after irradiation, swelling was the only morphological change present. In cells treated with Ab-IR700, similar swelling was observed at 5 min after irradiation. However, blebs formed on the plasma membrane of cells at 15 min (white arrows). Magnified images of cells treated with LMW-IR700 or Ab-IR700 clearly indicate different morphological changes induced at 30 min after irradiation. In addition, time-lapse movies of light-irradiated cells obviously show different morphological changes induced by LMW-IR700 (Supplementary video 1) and Ab-IR700 (Supplementary video 2). These results suggested that LWM-IR700 and Ab-IR700 induced different cell damage via different cytotoxic mechanisms.

3.3. Cytotoxicity induced by LMW-IR700 and Ab-IR700 assessed by PI-staining and MTT assay.

PI-stained dead cells were detected by fluorescence microscopy (Fig. 3B). Higher PI uptake was observed in cells treated with LMW-IR700 than Ab-IR700 when the duration of NIR light irradiation was 1 and 3 min. In cells treated with Ab-IR700 and irradiated with light for 5 min, fluorescence PI was observed in the cell nucleus and cytoplasm. Because PI emits intense fluorescence after it binds to nucleic acids such as DNA and RNA, this indicated that nucleic acid had leaked out of the nucleus in cells treated with Ab-IR700.

Subsequently, we performed the quantitative analysis of cytotoxicity using an MTT assay (Fig. 3C). The viability of cells treated with conjugates alone or light alone was not decreased compared with control cells. However, the viability of cells treated with both conjugates together and light irradiation was decreased in a light dose dependent manner. However, there was no significant difference in cytotoxicity in cells treated with LMW-IR700 or Ab-IR700.

3.4. LMW-IR700 is internalized into cells at a greater rate than Ab-IR700 over the same incubation time.

We investigated the subcellular localization of LMW-IR700 and Ab-IR700 (Fig. 3D). Confocal microscopic images show that large amounts of LMW-IR700 were

internalized by endocytosis and accumulated in the cells. Although LMW-IR700 was partly localized on lysosomes stained with LysoTracker Green, IR700 fluorescence signals were observed throughout the cells except for the nuclei. Compared with LMW-IR700, a lower accumulation of Ab-IR700 was observed, which was localized on plasma membranes (white arrows) and lysosomes (yellow arrow heads). These results clearly indicate that the uptake and subcellular localization of LMW-IR700 and Ab-IR700 are markedly different.

3.5. LMW-IR700 induces cell death accompanied by bleb formation, a hallmark of NIR-PIT with Ab-IR700, under conditions related to ROS and subcellular localization.

Next, we investigated how enzyme reactions, ROS, and the subcellular localization of conjugates influenced cytotoxicity induced by LMW-IR700 and Ab-IR700. Fig. 4A shows that LMW-IR700 and Ab-IR700 induced cell death at 4°C and 37°C during NIR light exposure, suggesting that the cell damage induced by LMW-IR700 and Ab-IR700 does not require enzyme reactions. Fig. 4B shows the microscopic images of treated cells in the presence of 1 or 10 mM NaN_3, a general $^1O_2$ quencher. When NaN_3 was added to the culture medium, bleb formation was observed

in cells treated with LMW-IR700, whose morphological changes were the same as those in cells treated with Ab-IR700 shown in Fig. 3A. In cells treated with Ab-IR700 in the presence of NaN_3, cell damage was not changed and bleb formation and cell swelling were observed. Fig. 4C shows the influence of the subcellular localization of the conjugates. In this experiment, the internalization of conjugates via endocytosis was inhibited at 4°C so that LMW-IR700 and Ab-IR700 were localized only on the plasma membrane. We observed similar morphological changes including bleb formation and swelling in cells treated with LMW-IR700 and Ab-IR700. These findings suggested that the mechanism of cell damage was changed when ROS was quenched by NaN_3 and when LMW-IR700 was localized only on the plasma membrane.

3.6. The water-soluble axial-ligand of LMW-IR700 is cleaved after NIR light exposure.

Changes in the chemical structure of LMW-IR700 after NIR light irradiation were analyzed. HPLC analyses indicated more hydrophobic products (LMW-IR700-1 and LMW-IR700-2) were generated from LMW-IR700 after light irradiation (10 J/cm^2) under electron donor (cysteine) added and deoxygenated conditions (Fig. 5A

and C). To evaluate the photolysis of LWM-IR700 quantitatively, methylene blue was added to the sample as an exogenous standard, and its retention time was approximately 8.3 min. Fig. 5B shows the results of the quantitative analysis of the photolysis of LMW-IR700. A decrease of LMW-IR700 was observed only when the agents were irradiated with NIR light (2 J/cm^2) under the cysteine added and deoxygenated conditions. We also demonstrated that the photoinduced decomposition depended on the concentration of cysteine. The degradation product fractions were sampled and the chemical structure was confirmed by MS. Taken together, these results indicated that the water-soluble axial-ligand of LMW-IR700 was cleaved with NIR light irradiation, yielding more hydrophobic LMW-IR700-1 and LMW-IR700-2 products (Fig. 5C).

4. Discussion

A targeting moiety cannot deliver cargo (e.g., a drug) to an appropriate site when the cargo is too large compared with the size of the targeting molecule because the chemical and/or biological characteristics of the conjugates, including the binding affinity, might be influenced by the cargo's properties including hydrophilicity and charge (Garland et al., 2016)(Bordenave et al., 2016)(Janzer et al., 2016)(Kumar et al., 2019). Because the targeting moiety of LMW-IR700 (MW ~300) is relatively smaller than that of IR700 (MW ~2,000), the function of LMW ligands might be influenced. However, LMW-IR700 selectively bound to PSMA-positive LNCaP cells and cell death was induced after NIR light irradiation (Fig. 2) due to the high hydrophilicity of IR700, and i*n vivo* therapeutic effects were exhibited in LMW-IR700-treated mice (Fig. S2). Furthermore, it was reported that the LMW ligand targeting PSMA used in this study delivered radionuclide-chelate complexes, which are a relatively large cargo (Wüstemann et al., 2019), and our data is consistent with previous reports on LWM-IR700 (Wang et al., 2016)(Chen et al., 2017).

In this study, differences in cytotoxicity and the cytotoxic mechanisms of LMW-IR700 and Ab-IR700 were investigated. Fig. 3B shows a higher uptake of PI at 60 min after light irradiation in cells treated with LMW-IR700 compared with Ab-

IR700 when the irradiation time was 1 or 3 min. However, there was no significant difference in cytotoxicity quantitatively assessed with an MTT assay performed 24 h after light exposure (Fig. 3C). These results indicated that both LMW-IR700 and Ab-IR700 eventually decreased cell viability to the same degree, although the process of cell death and/or its rate of progression were different. Microscopic analysis demonstrated swelling and bleb formation in cells treated with Ab-IR700 (Fig. 3A). These morphological alterations were also observed in various cell lines after treatment with NIR-PIT with Ab-IR700 (Mitsunaga et al., 2012)(Nagaya et al., 2017b)(Nakajima et al., 2018a). In contrast to Ab-IR700, bleb formation was not detected in cells treated with LMW-IR700 and only cell swelling was induced after NIR light irradiation. Collectively, different morphological changes were observed in cells treated with LMW-IR700 and Ab-IR700, suggesting LMW-IR700 and Ab-IR700 induce cell damage via different cytotoxic mechanisms.

In NIR-PIT with Ab-IR700, IR700 aggregates on the plasma membrane and induces physical membrane damage, leading to immunogenic cell death, which does not require enzyme reactions or ROS-mediated damage (Mitsunaga et al., 2011)(Sato et al., 2018)(Nakajima et al., 2018b). Fig. 4A suggested that cell damage induced by LMW-IR700 and Ab-IR700 does not require enzyme reactions, because morphological

changes were also induced at 4°C. We next investigated the influence of ROS on cell damage. Fig. S3 showed that LMW-IR700 produced ROS after NIR light irradiation. In Fig. 4B, bleb formation was observed in cells treated with LMW-IR700 in the presence of NaN_3, known as a $^1O_2$ quencher, and the morphological changes were consistent with those induced by Ab-IR700. Thus, LMW-IR700 usually induces $^1O_2$-mediated cell death accompanied by cell swelling, but the cellular damage with bleb formation induced by the aggregations was the main factor under $^1O_2$-quenched conditions. In contrast, the morphological changes induced by Ab-IR700 were not affected by the addition of 1 and 10 mM NaN_3 (Fig. 4B), showing that $^1O_2$ did not induce plasma membrane damage in the Ab-IR700 treated cells.

We consider that the subcellular localization of conjugates was responsible for the difference in the main cytotoxic mechanism between LMW-IR700 and Ab-IR700 (Nakajima and Ogawa, 2020). Fig. 3D shows that LMW-IR700 accumulated to a greater degree than Ab-IR700 with the same incubation time, because the rate of internalization was faster for LMW-IR700 than Ab-IR700. Furthermore, the fluorescent signals of LMW-IR700 were detected throughout cells except for the nuclei. When the cells were exposed to NIR light under the conditions where LMW-IR700 was localized only on the plasma membrane by inhibiting endocytosis at 4°C, the induction of bleb formation, a

hallmark of NIR-PIT with Ab-IR700, was observed (Fig. 4C). In addition, the release of water-soluble axial ligands of LMW-IR700 was observed, consistent with a previous report on Ab-IR700 (Fig. 5) (Sato et al., 2018)(Fujimura et al., 2020). These results suggested that the binding of LMW-IR700 to the plasma membrane induces membrane damage via aggregation similar to Ab-IR700. During this process, the acute and intensive damage to the plasma membrane induces bleb formation (Ogata et al., 2017), whereas the internalized LMW-IR700 might induce cell swelling by promoting the ROS-mediated damage of various cellular organelles including the cytoskeleton throughout the cells. The rate of internalization and subcellular localization of LMW-IR700 could be controlled by conjugation with large molecules, and thus there is room to develop drugs with better kinetics. In addition to the rate of internalization, conjugates with a lower binding affinity are retained on the plasma membrane to a lower degree compared with conjugates with a higher affinity. Indeed, the affinity of an antibody (K_d < 1 nM) is about 10 times greater than that of LMW ligands (K_d ~10 nM) against PSMA (Wüstemann et al., 2019)(Tykvart et al., 2014), indicating Ab-IR700 is retained on the membrane to a greater degree than LMW-IR700. Thus, a smaller amount of LMW-IR700 bound to the plasma membrane cannot induce damage to the cell membrane by forming aggregates. To further elucidate the relationship between

membrane damage and the amount of LMW-IR700 on plasma membrane, cells were incubated with LMW-IR700 at tenfold concentration and irradiated with light (Fig. S4). However, aggregation-mediated morphological changes were not observed. This would be because the increased concentration did not change the amount of LMW-IR700 bound to the membrane, since internalization of LMW-IR700 is quite rapid. Taken together, these findings suggest that the subcellular localization of conjugates determines whether aggregation or ROS is the major cytotoxic mechanism in cells treated with IR700-conjugates.

5. Conclusions

The main cytotoxic mechanisms of conjugates were altered when different targeting molecules such as antibodies and LMW ligands were used to deliver IR700. The ROS-mediated effect was the main mechanism promoted by LMW-IR700 in this study, but cytotoxicity induced by aggregation was also observed under some conditions related to ROS and subcellular localization. Thus, in the case of LMW-IR700, cytotoxicity is caused by ROS as well as by aggregation.

Acknowledgements

This work was supported by the Japan Science and Technology Agency (JST) CREST Grant Number JPMJCR1902; JSPS KAKENHI Grant Number 19H03593; JSPS Grant-in-Aid for JSPS Fellows Grant Numbers 20J12988 and 20J22962; the Photo-excitonix Project in Hokkaido University; the Uehara Memorial Foundation; and the Nagai Memorial Research Scholarship from the Pharmaceutical Society of Japan. This work was partly supported by a MEXT Project for promoting public utilization of advanced research infrastructure (Program for Supporting Introduction of the New Sharing System) Grant Number JPMXS0420100120; the Platform Project for Supporting in Drug Discovery and Life Science Research (Platform for Drug Discovery, Informatics, and Structural Life Science) from the Japan Agency for Medical Research and Development (AMED); and a Platform Project for Supporting Drug Discovery and Life Science Research (Basis for Supporting Innovative Drug Discovery and Life Science Research (BINDS)) from AMED under Grant Number JP19am0101093. We thank Instrumental Analysis Division, Global Facility Center, Creative Research Institution, Hokkaido University for ESI-MS with an Exactive Mass Spectrometer and providing insight and expertise that greatly assisted the research.

Disclosure statement

Mikako Ogawa receives research funding from Rakuten Medical Japan, K.K. (Tokyo, Japan). The funder was not involved in the study design, analysis, and interpretation of the data.

Author contributions

Kohei Nakajima: Investigation, Visualization, Writing - original draft.

Fuka Miyazaki: Investigation, Visualization, Writing - original draft.

Kazuki Terada: Investigation.

Hideo Takakura: Investigation, Writing - review & editing.

Motofumi Suzuki: Investigation.

Mikako Ogawa: Conceptualization, Funding acquisition, Resources, Supervision, Writing - review & editing.

References

Bordenave, T., Helle, M., Beau, F., Georgiadis, D., Tepshi, L., Bernes, M., Ye, Y., Levenez, L., Poquet, E., Nozach, H., Razavian, M., Toczek, J., Stura, E.A., Dive, V., Sadeghi, M.M., Devel, L., 2016. Synthesis and in Vitro and in Vivo Evaluation of MMP-12 Selective Optical Probes. Bioconjug. Chem. 27, 2407–2417. https://doi.org/10.1021/acs.bioconjchem.6b00377

Chen, Y., Chatterjee, S., Lisok, A., Minn, I., Pullambhatla, M., Wharram, B., Wang, Y., Jin, J., Bhujwalla, Z.M., Nimmagadda, S., Mease, R.C., Pomper, M.G., 2017. A PSMA-targeted theranostic agent for photodynamic therapy. J. Photochem. Photobiol. B Biol. 167, 111–116. https://doi.org/10.1016/j.jphotobiol.2016.12.018

Choy, C.J., Berkman, C.E., 2016. A Method to Determine the Mode of Binding for GCPII Inhibitors using Bio-Layer Interferometry. J Enzym. Inhib Med Chem. 31, 1690–1693. https://doi.org/10.3109/14756366.2015.1132208.A

Dolmans, D.E.J.G.J., Fukumura, D., Jain, R.K., 2003. Photodynamic therapy for cancer. Nat. Rev. Cancer 3, 380–387. https://doi.org/10.1016/j.semcancer.2003.11.001

Dou, X., Nomoto, T., Takemoto, H., Matsui, M., Tomoda, K., Nishiyama, N., 2018. Effect of multiple cyclic RGD peptides on tumor accumulation and intratumoral distribution of IRDye 700DX-conjugated polymers. Sci. Rep. 8, 1–12.

https://doi.org/10.1038/s41598-018-26593-0

Fujimura, D., Inagaki, F., Okada, R., Rosenberg, A., Furusawa, A., Choyke, P.L., Kobayashi, H., 2020. Conjugation Ratio, Light Dose, and pH Affect the Stability of Panitumumab-IR700 for Near-Infrared Photoimmunotherapy. ACS Med. Chem. Lett. 11, 1598–1604. https://doi.org/10.1021/acsmedchemlett.0c00262

Garland, M., Yim, J.J., Bogyo, M., 2016. Bright future for precision medicine: advances in fluorescent chemical probe design and their clinical application. Cell Chem. Biol. 23, 122–136. https://doi.org/10.1016/j.chembiol.2015.12.003

Henninot, A., Collins, J.C., Nuss, J.M., 2018. The Current State of Peptide Drug Discovery: Back to the Future? J. Med. Chem. 61, 1382–1414. https://doi.org/10.1021/acs.jmedchem.7b00318

Janzer, M., Larbig, G., Kübelbeck, A., Wischnjow, A., Haberkorn, U., Mier, W., 2016. Drug Conjugation Affects Pharmacokinetics and Specificity of Kidney-Targeted Peptide Carriers. Bioconjug. Chem. 27, 2441–2449. https://doi.org/10.1021/acs.bioconjchem.6b00397

Kobayashi, H., Choyke, P.L., 2019. Near-Infrared Photoimmunotherapy of Cancer. Acc. Chem. Res. 52, 2332–2339. https://doi.org/10.1021/acs.accounts.9b00273

Kobayashi, M., Harada, M., Takakura, H., Ando, K., Goto, Y., Tsuneda, T., Ogawa, M.,

Taketsugu, T., 2020. Theoretical and Experimental Studies on the Near-Infrared Photoreaction Mechanism of a Silicon Phthalocyanine Photoimmunotherapy Dye: Photoinduced Hydrolysis by Radical Anion Generation. Chempluschem 85, 1–6. https://doi.org/10.1002/cplu.202000338

Kumar, P., Tripathi, S.K., Chen, C.P., Wickstrom, E., Thakur, M.L., 2019. Evaluating Ga-68 Peptide Conjugates for Targeting VPAC Receptors: Stability and Pharmacokinetics. Mol. Imaging Biol. 21, 130–139. https://doi.org/10.1007/s11307-018-1207-x

Mao, C., Zhao, Y., Li, F., Li, Z., Tian, S., Debinski, W., Ming, X., 2018. P-glycoprotein targeted and near-infrared light-guided depletion of chemoresistant tumors. J. Control. Release 286, 289–300. https://doi.org/10.1016/j.jconrel.2018.08.005

Mitsunaga, M., Nakajima, T., Sano, K., Kramer-Marek, G., Choyke, P.L., Kobayashi, H., 2012. Immediate in vivo target-specific cancer cell death after near infrared photoimmunotherapy. BMC Cancer 12, 345. https://doi.org/10.1186/1471-2407-12-345

Mitsunaga, M., Ogawa, M., Kosaka, N., Rosenblum, L.T., Choyke, P.L., Kobayashi, H., 2011. Cancer cell–selective in vivo near infrared photoimmunotherapy targeting specific membrane molecules. Nat. Med. 17, 1685–1691.

https://doi.org/10.1038/nm.2554

Morales-Cruz, M., Delgado, Y., Castillo, B., Figueroa, C.M., Molina, A.M., Torres, A., Milián, M., Griebenow, K., 2019. Smart targeting to improve cancer therapeutics. Drug Des. Devel. Ther. 13, 3753–3772. https://doi.org/10.2147/DDDT.S219489

Nagaya, T., Nakamura, Y., Okuyama, S., Ogata, F., Maruoka, Y., Choyke, P.L., Kobayashi, H., 2017a. Near-Infrared Photoimmunotherapy Targeting Prostate Cancer with Prostate-Specific Membrane Antigen (PSMA) Antibody. Mol. Cancer Res. 15, 1153–1162. https://doi.org/10.1158/1541-7786.MCR-17-0164

Nagaya, T., Nakamura, Y., Sato, K., Harada, T., Choyke, P.L., Hodge, J.W., Schlom, J., Kobayashi, H., 2017b. Near infrared photoimmunotherapy with avelumab, an anti-programmed death-ligand 1 (PD-L1) antibody. Oncotarget 8, 8807–8817. https://doi.org/10.18632/oncotarget.12410

Nagaya, T., Nakamura, Y., Sato, K., Harada, T., Choyke, P.L., Kobayashi, H., 2016. Near infrared photoimmunotherapy of B-cell lymphoma. Mol. Oncol. 10, 1404–1414. https://doi.org/10.1016/j.molonc.2016.07.010

Nakajima, K., Kimura, T., Takakura, H., Yoshikawa, Y., Kameda, A., Shindo, T., Sato, K., Kobayashi, H., Ogawa, M., 2018a. Implantable wireless powered light emitting diode (LED) for near-infrared photoimmunotherapy: device development and

experimental assessment in vitro and in vivo. Oncotarget 9, 20048–20057.

Nakajima, K., Ogawa, M., 2020. Phototoxicity in near-infrared photoimmunotherapy is influenced by the subcellular localization of antibody-IR700. Photodiagnosis Photodyn. Ther. 31, 101926. https://doi.org/10.1016/j.pdpdt.2020.101926

Nakajima, K., Takakura, H., Shimizu, Y., Ogawa, M., 2018b. Changes in plasma membrane damage inducing cell death after treatment with near-infrared photoimmunotherapy. Cancer Sci. 109, 2889–2896. https://doi.org/10.1111/cas.13713

Nishimura, T., Mitsunaga, M., Sawada, R., Saruta, M., Kobayashi, H., Matsumoto, N., Kanke, T., Yanai, H., Nakamura, K., 2019. Photoimmunotherapy targeting biliary-pancreatic cancer with humanized anti-TROP2 antibody. Cancer Med. 1–12. https://doi.org/10.1002/cam4.2658

Ogata, F., Nagaya, T., Okuyama, S., Maruoka, Y., Choyke, P.L., Yamauchi, T., Kobayashi, H., 2017. Dynamic changes in the cell membrane on three dimensional low coherent quantitative phase microscopy (3D LC-QPM) after treatment with the near infrared photoimmunotherapy. Oncotarget 8, 104295–104302. https://doi.org/http://dx.doi.org/10.18632/oncotarget.22223

Sato, K., Ando, K., Okuyama, S., Moriguchi, S., Ogura, T., Totoki, S., Hanaoka, H.,

Nagaya, T., Kokawa, R., Takakura, H., Nishimura, M., Hasegawa, Y., Choyke, P.L., Ogawa, M., Kobayashi, H., 2018. Photoinduced ligand release from a silicon phthalocyanine dye conjugated with monoclonal antibodies: a mechanism of cancer cell cytotoxicity after near-infrared photoimmunotherapy. ACS Cent. Sci. 4, 1559–1569. https://doi.org/10.1021/acscentsci.8b00565

Tykvart, J., Navrátil, V., Sedlák, F., Corey, E., Colombatti, M., Fracasso, G., Koukolík, F., Bařinka, C., Šácha, P., Konvalinka, J., 2014. Comparative analysis of monoclonal antibodies against prostate-specific membrane antigen (PSMA). Prostate 74, 1674–1690. https://doi.org/10.1002/pros.22887

Wang, X., Tsui, B., Ramamurthy, G., Zhang, P., Meyers, J., Kenney, M.E., Kiechle, J., Ponsky, L., Basilion, J.P., 2016. Theranostic Agents for Photodynamic Therapy of Prostate Cancer by Targeting Prostate-Specific Membrane Antigen. Mol. Cancer Ther. 15, 1834–1844. https://doi.org/10.1158/1535-7163.MCT-15-0722

Wei, W., Jiang, D., Ehlerding, E.B., Barnhart, T.E., Yang, Y., Engle, J.W., Luo, Q.Y., Huang, P., Cai, W., 2019. CD146-targeted multimodal image-guided photoimmunotherapy of melanoma. Adv. Sci. 6, 181237. https://doi.org/10.1002/advs.201801237

Wüstemann, T., Haberkorn, U., Babich, J., Mier, W., 2019. Targeting prostate cancer:

Prostate-specific membrane antigen based diagnosis and therapy. Med. Res. Rev. 39, 40–69. https://doi.org/10.1002/med.21508

Yoo, J.O., Ha, K.S., 2012. New Insights into the Mechanisms for Photodynamic Therapy-Induced Cancer Cell Death. Int. Rev. Cell Mol. Biol. 295, 139–174. https://doi.org/10.1016/B978-0-12-394306-4.00010-1

Figure legends

Figure 1. Synthesis of LMW-IR700 and Ab-IR700. (A) The PSMA-targeting LMW ligand composed of Glu-Urea-Lys was conjugated with IR700. (B) Anti-PSMA monoclonal Ab was conjugated with IR700. The number of IR700 bound to a single Ab was approximately three. r.t., room temperature.

Figure 2. Specific uptake of LMW-IR700 and cell death after NIR light irradiation. (A) PSMA-positive LNCaP and PSMA-negative DU145 cells were incubated with LMW-IR700 for 1 h at 37°C. IR700 fluorescence was observed by fluorescence microscopy. LMW-IR700 was taken into LNCaP cells but not into DU145 cells. (B) LNCaP cells were incubated with LMW-IR700 for 1 h at 37°C and then irradiated with NIR light. Cell death was only observed in cells treated with both LMW-IR700 and NIR light irradiation at post irradiation (lower right). Other control cells were not damaged. Scale bar: 50 μm.

Figure 3. Comparison of cytotoxicity and subcellular localization between LMW-IR700 and Ab-IR700. (A) Morphological changes were observed after NIR light irradiation. Swelling was induced in cells treated with LMW-IR700. Both cell swelling and bleb

formation were induced in cells treated with Ab-IR700. Scale bar: 50 μm. (B) The uptake of PI, which indicates a damaged plasma membrane, was observed by fluorescence microscopy. Scale bar: 50 μm. (C) Cell viability was evaluated with an MTT assay. A combination of conjugates and light decreased cell viability, but there was no significant difference in cytotoxicity induced by LMW-IR700 or Ab-IR700. Data are the means ± SEM (n = 4). Statistical significance was determined by Student's *t*-test. (D) Subcellular localization of LMW-IR700 and Ab-IR700 after 1 h incubation at 37°C. Lysosomes were stained with LysoTracker Green. LMW-IR700 was observed throughout cells except for the nucleus and Ab-IR700 was localized on the plasma membrane (white arrows) and lysosomes (yellow arrow heads). Scale bar: 10 μm.

Figure 4. Microscopic observation of cells before and after NIR light irradiation (A) at 4°C or 37°C during irradiation (B) in the presence of 1 or 10 mM NaN_3 (C) under conditions where LMW-IR700 was localized only on the plasma membrane. (A) No significant difference in morphological changes was observed at 4°C or 37°C in cells treated with LMW-IR700 or Ab-IR700. (B) Bleb formation and swelling was induced in cells treated with LMW-IR700 in the presence of NaN_3. (C) Similar morphological changes with bleb formation and cell swelling were induced by LMW-IR700 and Ab-

IR700 on the plasma membrane. Scale bar: 50 μm. (D) Confocal microscopic images show LMW-IR700 was internalized into cells to a greater degree than Ab-IR700. Scale bar: 20 μm.

Figure 5. Release of water-soluble axial-ligand of LMW-IR700 after NIR light irradiation. (A) The peak of LMW-IR700 was decreased and more hydrophobic degradation products (LMW-IR700-1, LMW-IR700-2) were observed in the HPLC chart in the irradiation (+) sample. (B) The photolysis of LMW-IR700 was quantitatively analyzed. The LMW-IR700 absorbance area was significantly decreased after NIR light irradiation when 5 mM cysteine was added under deoxygenated conditions. Data are the means ± SEM (n = 3). Statistical significance was determined by Student's *t*-test (*$p < 0.05$). (C) General schema of the photolysis of LMW-IR700. LMW-IR700-1 and LMW-IR700-2 were yielded after NIR light irradiation.

Figure 1

A

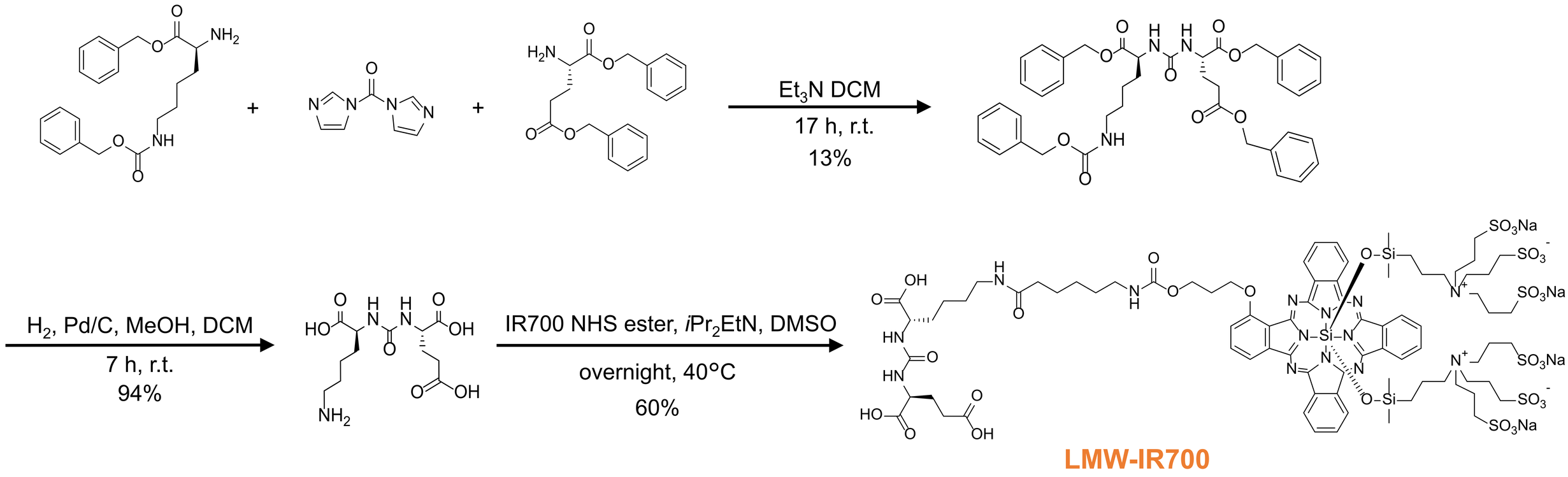
Et3N DCM
17 h, r.t.
13%
H2, Pd/C, MeOH, DCM
7 h, r.t.
94%
IR700 NHS ester, iPr2EtN, DMSO
overnight, 40°C
60%
LMW-IR700

B

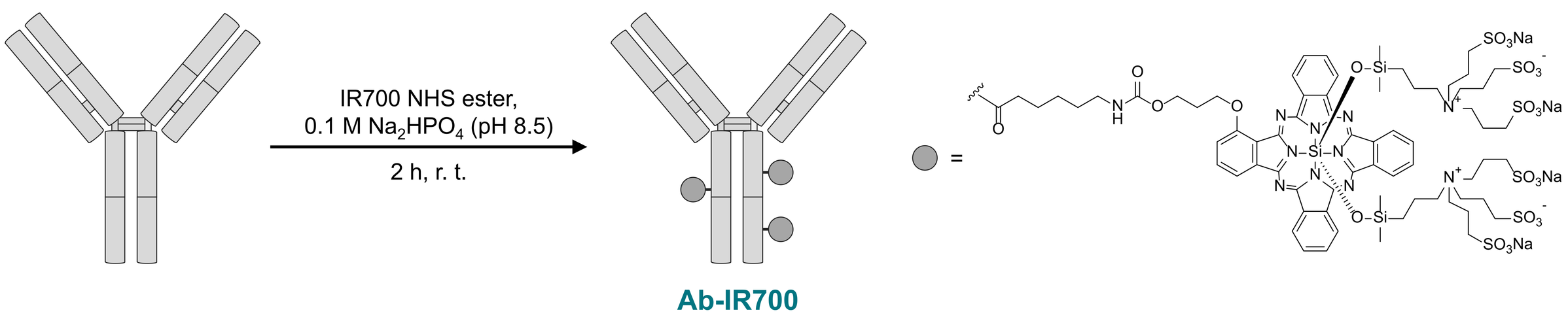
IR700 NHS ester,
0.1 M Na2HPO4 (pH 8.5)
2 h, r. t.
Ab-IR700
=

Figure 2

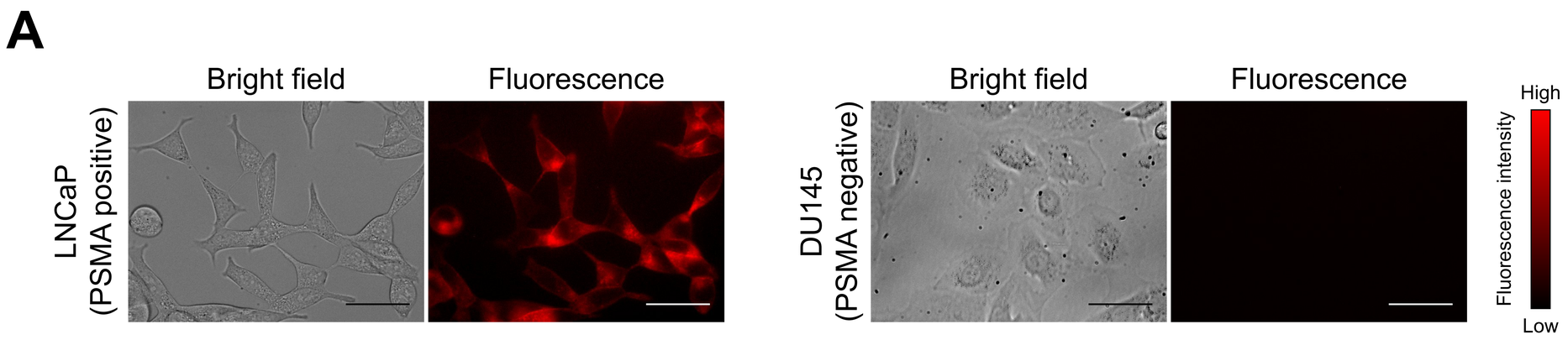
A
Bright field
Fluorescence
LNCaP
(PSMA positive)
Bright field
Fluorescence
DU145
(PSMA negative)
High
Fluorescence intensity
Low

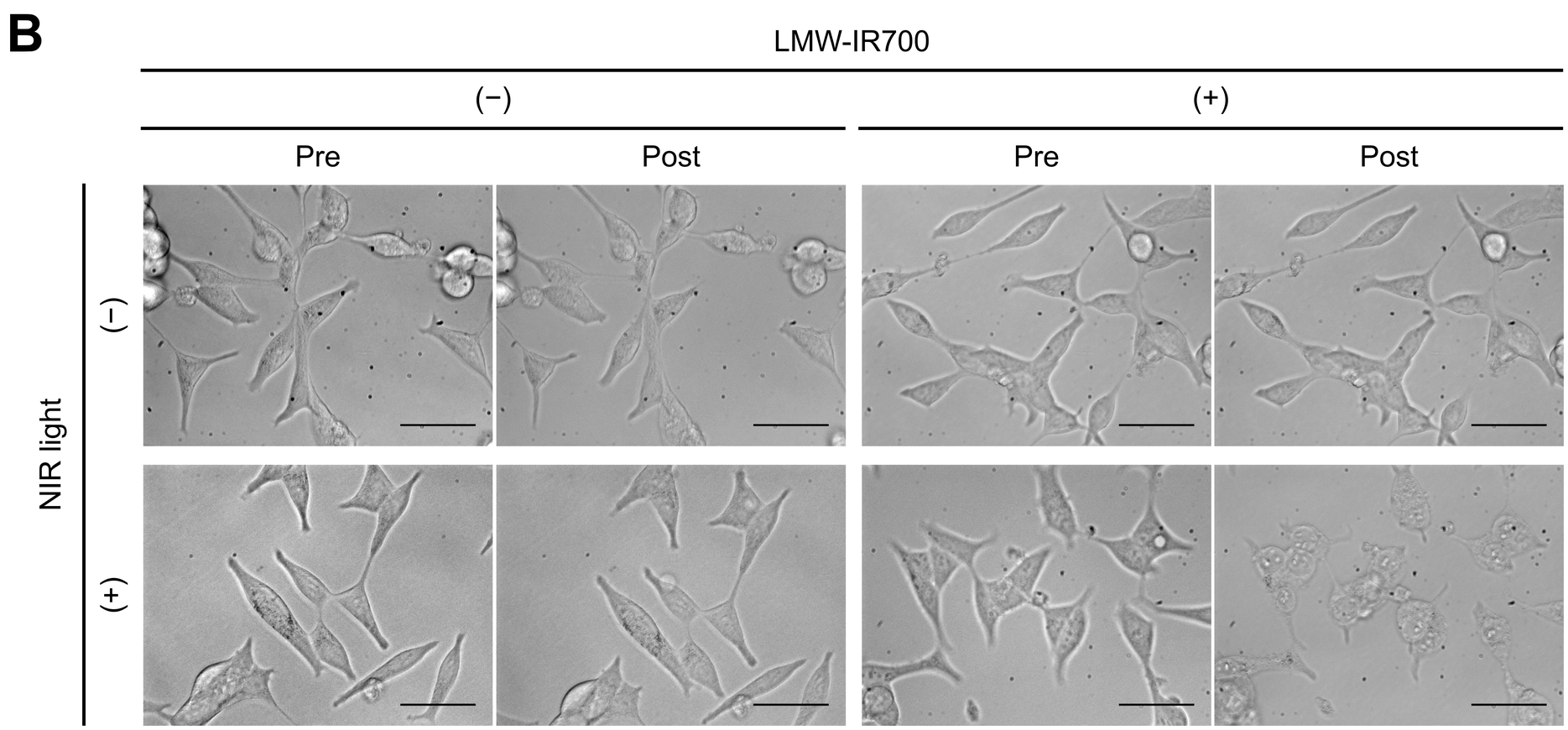
B
LMW-IR700
(−)
(+)
Pre
Post
Pre
Post
NIR light
(−)
(+)

Figure 3

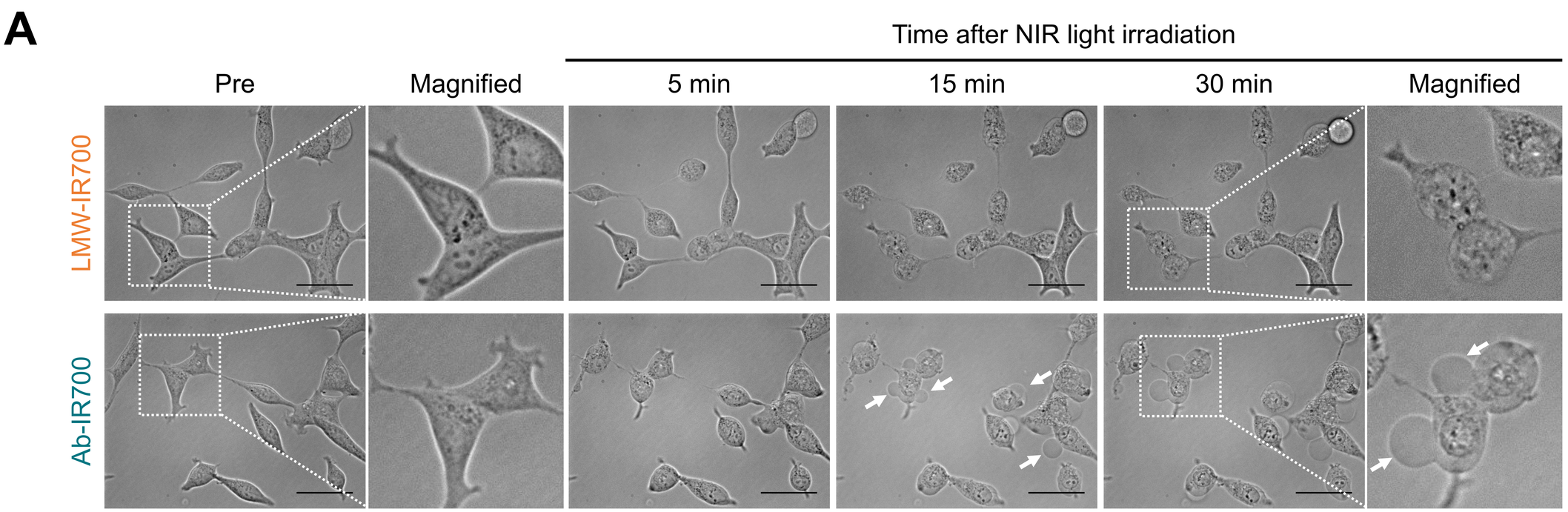
A
Time after NIR light irradiation
Pre
Magnified
5 min
15 min
30 min
Magnified
LMW-IR700
Ab-IR700

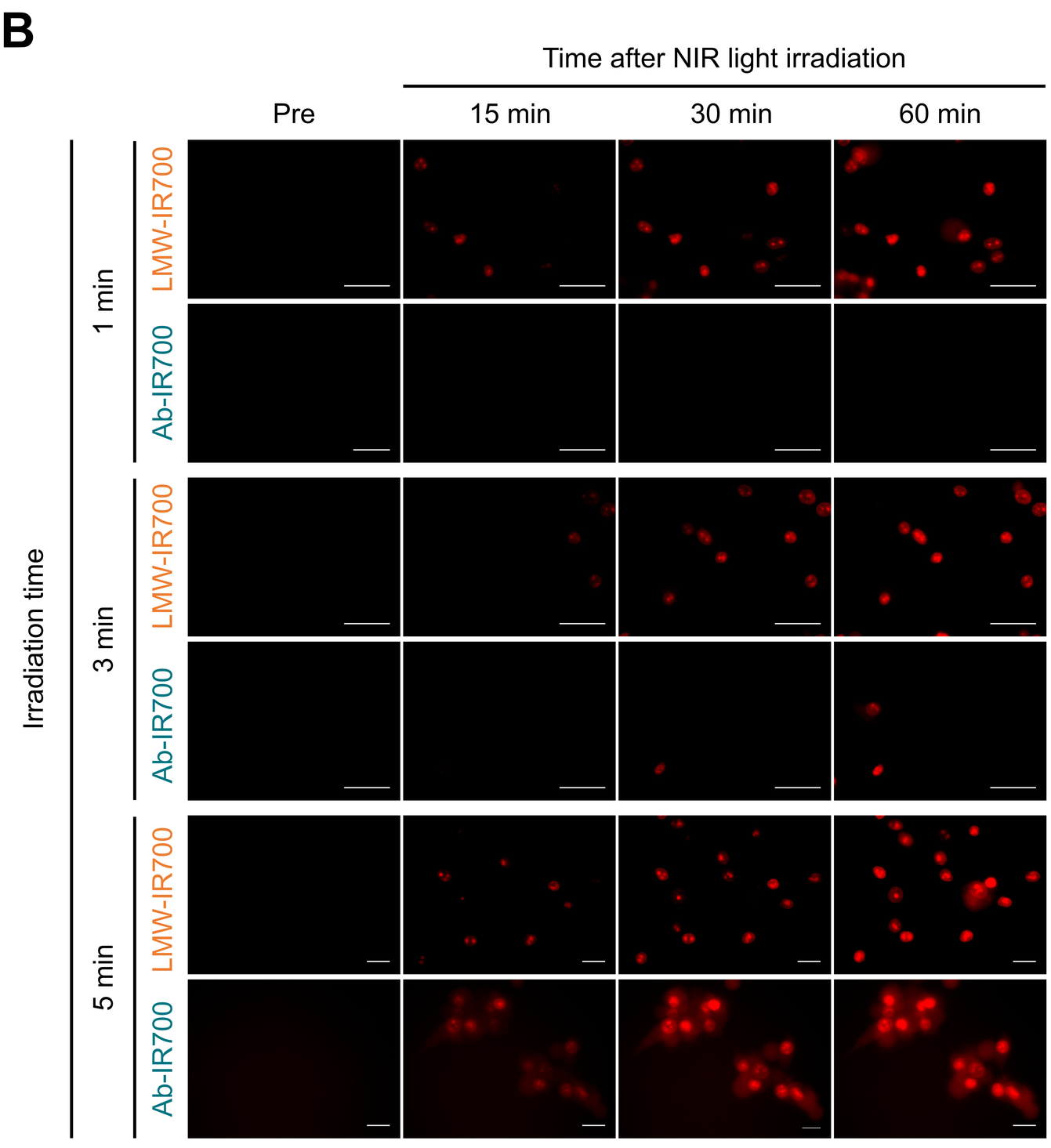
B
Time after NIR light irradiation
Pre
15 min
30 min
60 min
Irradiation time
1 min
3 min
5 min
LMW-IR700
Ab-IR700

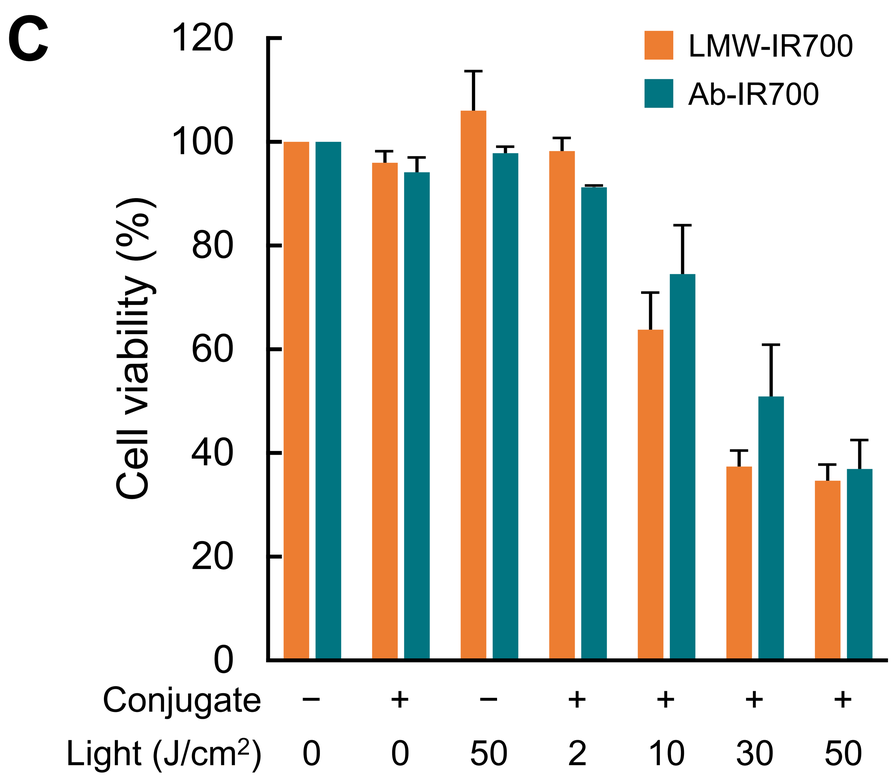
C
LMW-IR700
Ab-IR700
Cell viability (%)
120
100
80
60
40
20
0
Conjugate − + − + + + +
Light (J/cm2) 0 0 50 2 10 30 50

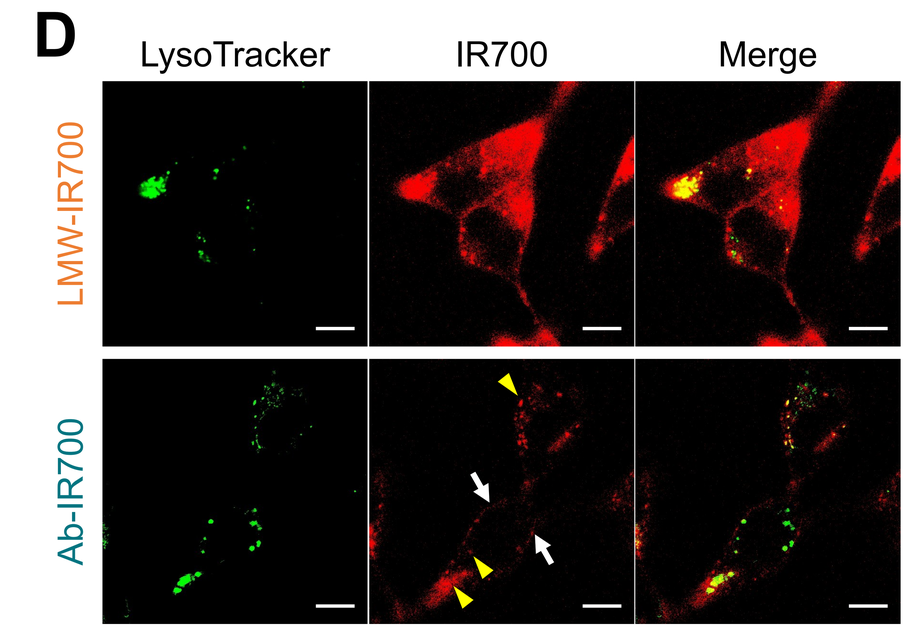
D
LysoTracker
IR700
Merge
LMW-IR700
Ab-IR700

Figure 4

A

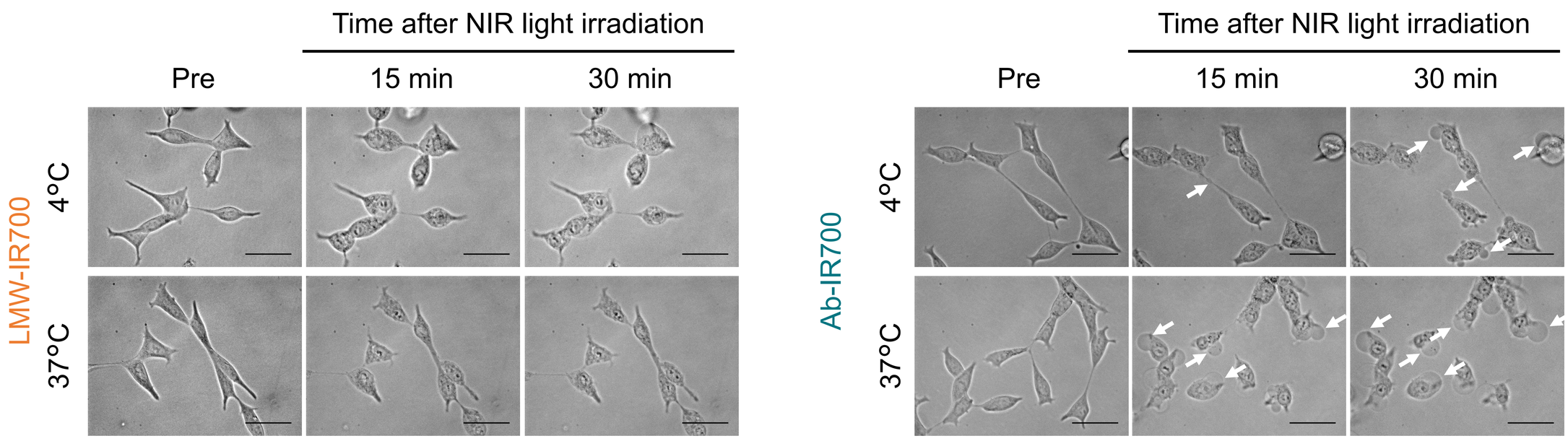
Time after NIR light irradiation
Pre
15 min
30 min
LMW-IR700
4°C
37°C
Time after NIR light irradiation
Pre
15 min
30 min
Ab-IR700
4°C
37°C

B

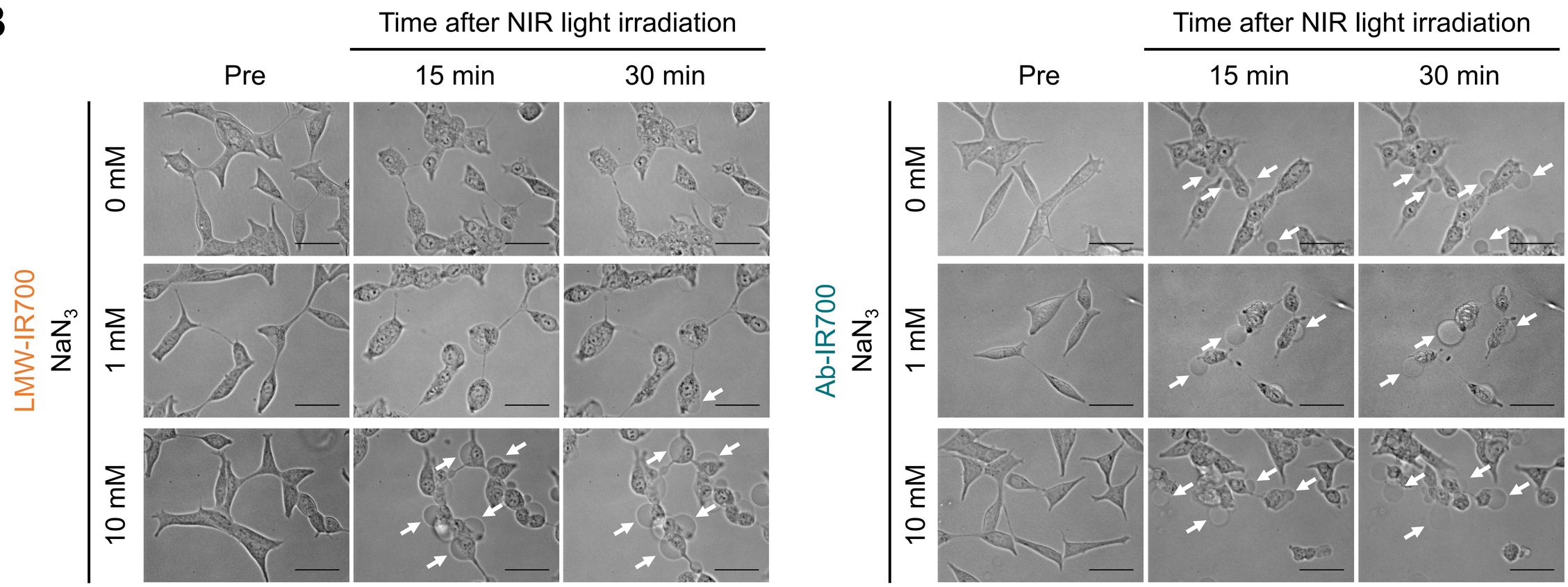
Time after NIR light irradiation
Pre
15 min
30 min
LMW-IR700
NaN3
0 mM
1 mM
10 mM
Time after NIR light irradiation
Pre
15 min
30 min
Ab-IR700
NaN3
0 mM
1 mM
10 mM

C

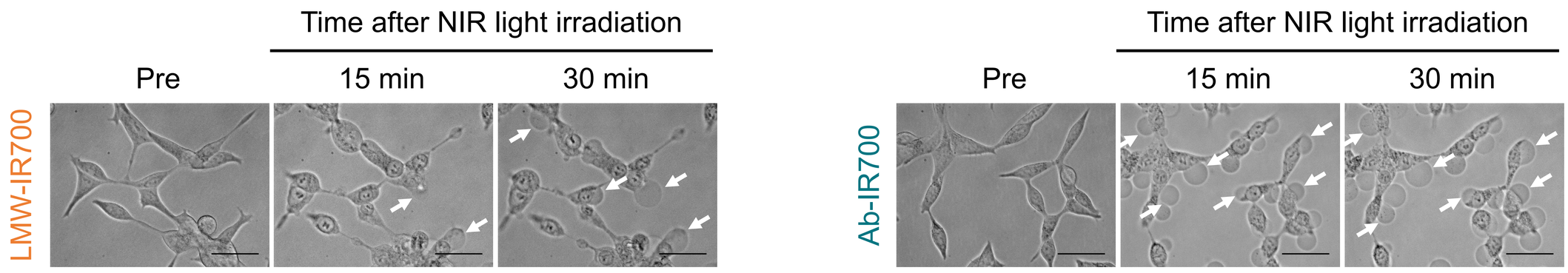
Time after NIR light irradiation
Pre
15 min
30 min
LMW-IR700
Time after NIR light irradiation
Pre
15 min
30 min
Ab-IR700

Figure 5

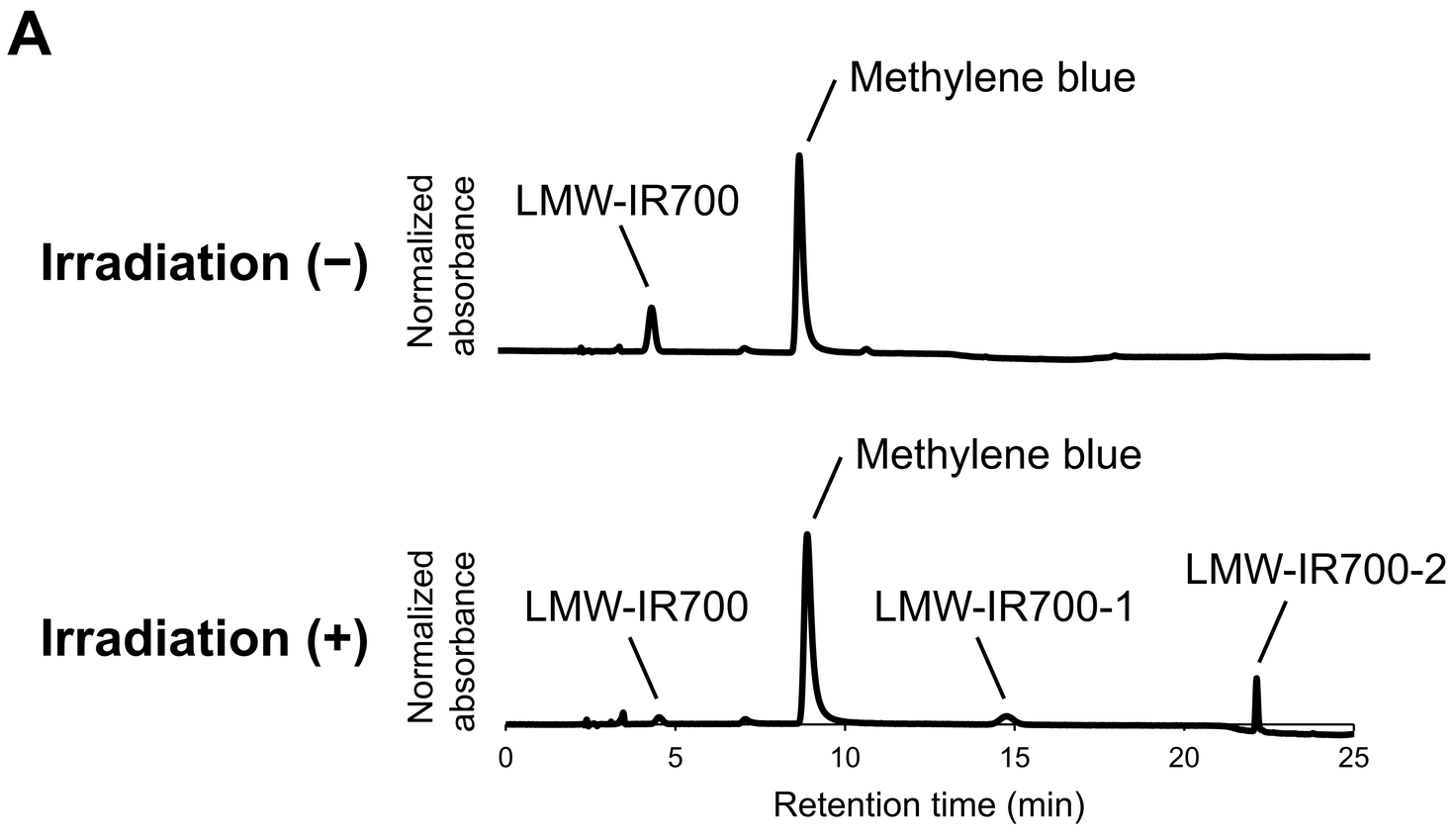
A
Irradiation (−)
Irradiation (+)
Normalized absorbance
LMW-IR700
Methylene blue
LMW-IR700-1
LMW-IR700-2
0
5
10
15
20
25
Retention time (min)

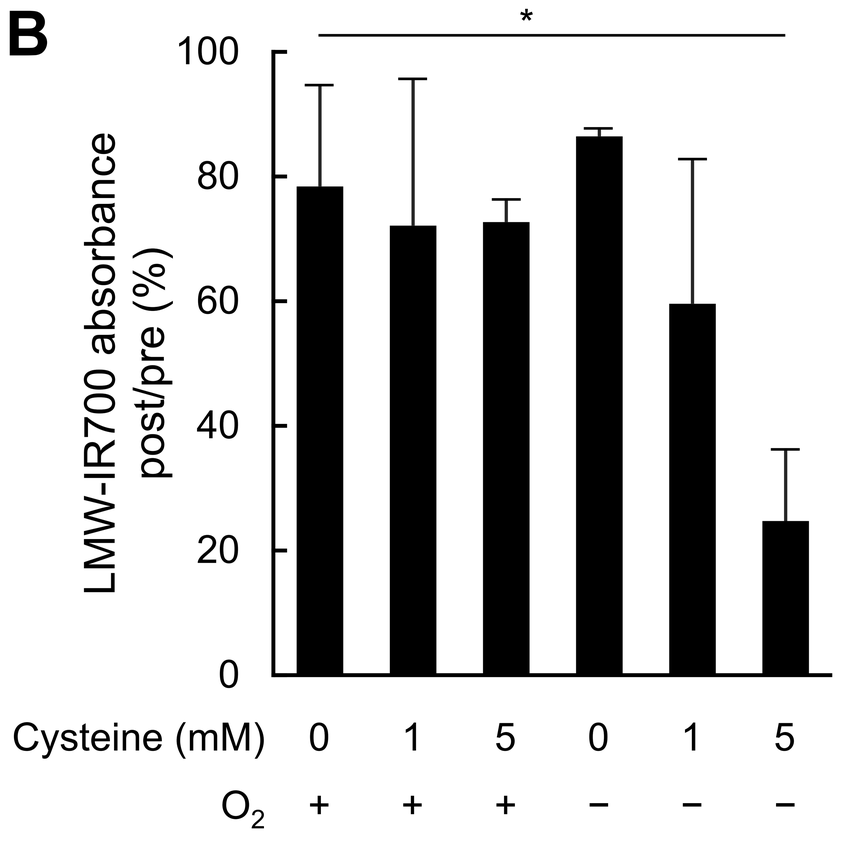
B
*
LMW-IR700 absorbance post/pre (%)
100
80
60
40
20
0
Cysteine (mM) 0 1 5 0 1 5
O2 + + + − − −

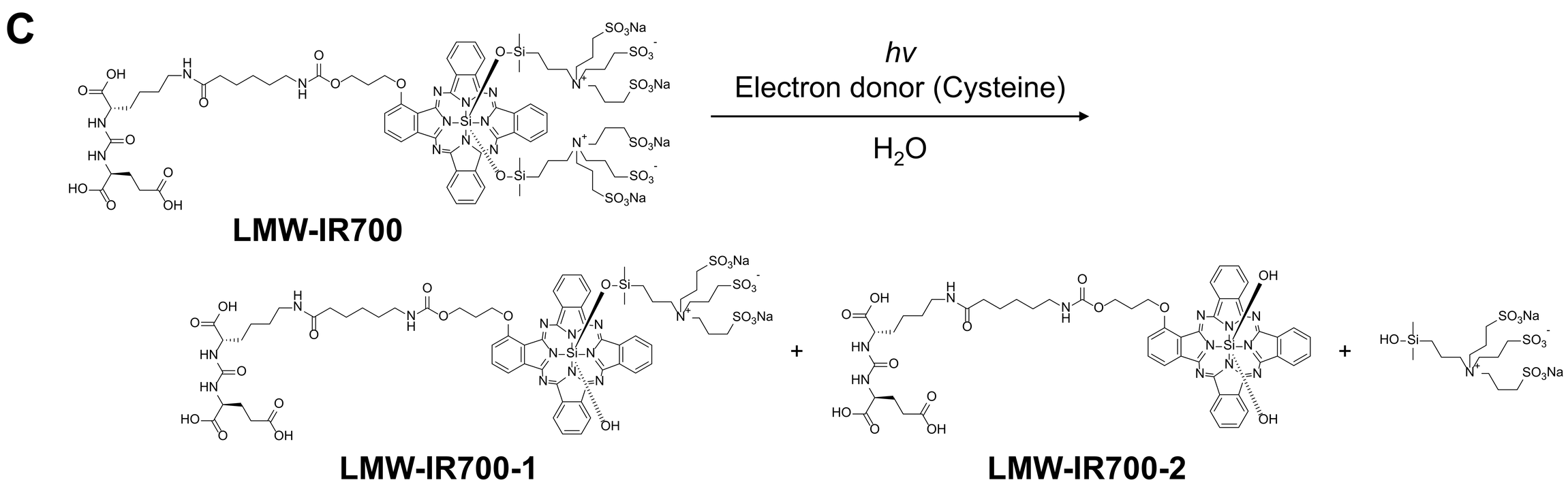
C
hv
Electron donor (Cysteine)
H2O
LMW-IR700
LMW-IR700-1
LMW-IR700-2

Supplementary data

Comparison of low-molecular-weight ligand and whole antibody in prostate-specific membrane antigen targeted near-infrared photoimmunotherapy

Kohei Nakajima, Fuka Miyazaki, Kazuki Terada, Hideo Takakura, Motofumi Suzuki, Mikako Ogawa

Supplementary Methods

Animal and Tumor model

All *in vivo* experiments were performed with approval from the Hokkaido University Animal Care Committee in accordance with the guidelines for the care and use of laboratory animals. Male 5-week-old CB17/Icr-*Prkdc*^{scid}/CrlCrlj (C. B-17 SCID) mice were from Charles River Laboratories Japan, Inc. (Yokohama, Japan). During the following procedures, mice were anesthetized with isoflurane.

LNCaP cells (8×10^6) suspended in 100 μL RPMI-1640/Matrigel (Corning Incorporated, NY, USA) (1/1, *v*/*v*) were injected subcutaneously in the dorsum. The mice were used for experiments after the tumor volume reached 150 mm^3. To measure the tumor volume, the greatest longitudinal diameter (length) and the greatest transversal diameter (width) of tumors were measured with a caliper. Tumor volume was calculated using the following equation: volume = length × $width^2$ × 0.5.

In vivo NIR-PIT with LMW-IR700

Tumor-bearing mice were randomized into 2 groups as follows: (1) no treatment (control); (2) LMW-IR700 injection followed with NIR light irradiation (NIR-PIT) (n = 3). To examine tumor uptake of LMW-IR700, tumors at 1h after injection of LMW-IR700 (5 nmol) were harvested, frozen, and sectioned. Samples were observed to detect IR700 fluorescence using BX41 microscope, which has a 670–745 nm excitation filter and a 769–849 nm emission filter.

To investigate therapeutic effects, the mice were intravenously injected with LMW-IR700 (5 nmol) on day 0, 2, and 4. One hour after the administration of LMW-IR700, tumor was irradiated with NIR light (MLL-III-690-800 mW; Changchun New Industries Optoelectronics Tech, Co., Ltd.) at 100 J/cm^2 (250 mW/cm^2).

Supplementary Figures

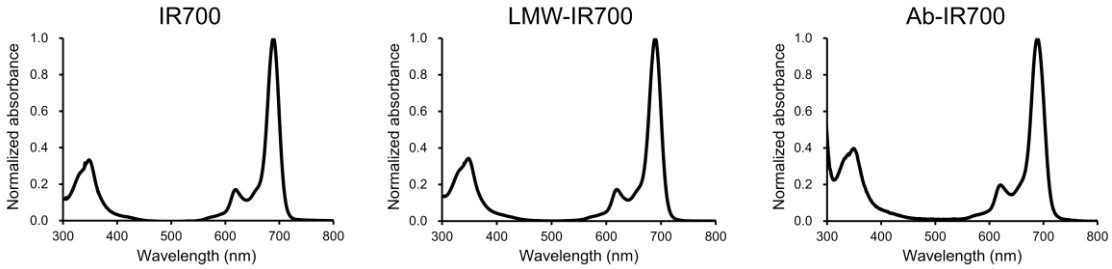

Figure S1. Absorption spectra of IR700, LMW-IR700, and Ab-IR700. Both LMW-IR700 and Ab-IR700 have a photo-absorption band in NIR region, showing that IR700 was surely conjugated to each molecule.

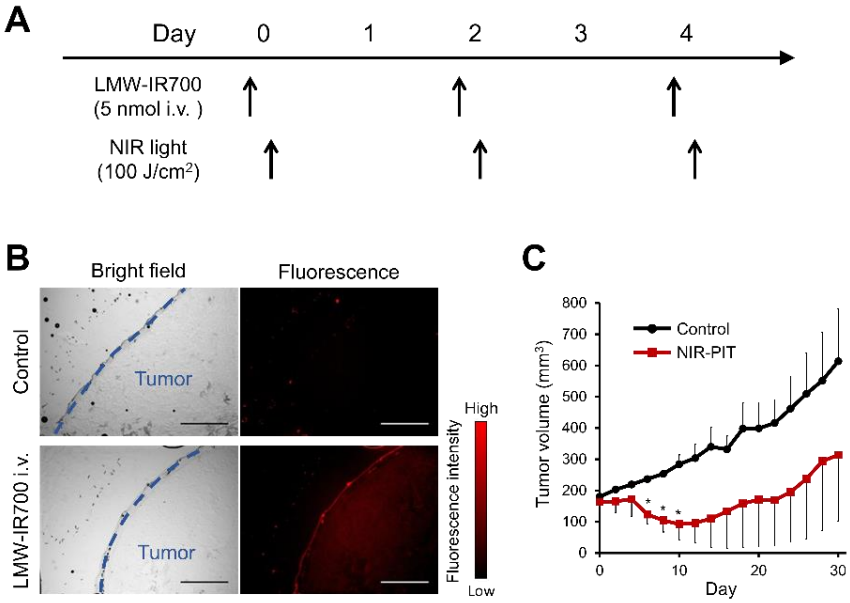

Figure S2. *In vivo* NIR-PIT with LMW-IR700. (A) Treatment schedule. Injection of LMW-IR700 and light irradiation were performed on day 0, 2, and 4. (B) Fluorescence microscopic images of tumor section. High signal of IR700 fluorescence showed the uptake of LMW-IR700. In bright field images, tumor and background sites are distinguished by blue dotted lines. Scale bar: 500 μm. (C) Changes in tumor volume in control and NIR-PIT-treated mice. NIR-PIT with LMW-IR700 significantly suppressed tumor growth compared with control mice. Data are the means ± SEM (n = 3). Statistical significance was determined by the Student's *t* test ($p < 0.05$).

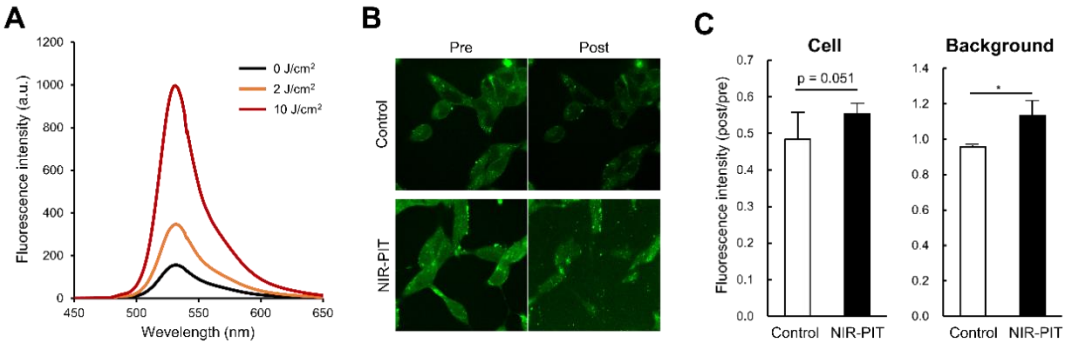

Figure S3. Evaluation of singlet oxygen production with fluorescent dye (singlet oxygen sensor green; SOSG). (A) Fluorescence spectra of aqueous solution (0.1 μM LMW-IR700, 10 μM SOSG) after NIR light irradiation (0, 2, 10 J/cm^2). Fluorescence intensity of SOSG was increased in a light dose-dependent manner, indicating that LMW-IR700 produced singlet oxygen. (B) Fluorescence microscopic images of cells incubated with SOSG. (C) Quantitative analysis shows changes in fluorescence intensity in cells and background area. These results suggest that LMW-IR700 produced singlet oxygen, although SOSG leaked out of cells. Data are the means ± SEM (n = 9). Statistical significance was determined by the Student's *t* test ($p < 0.05$).

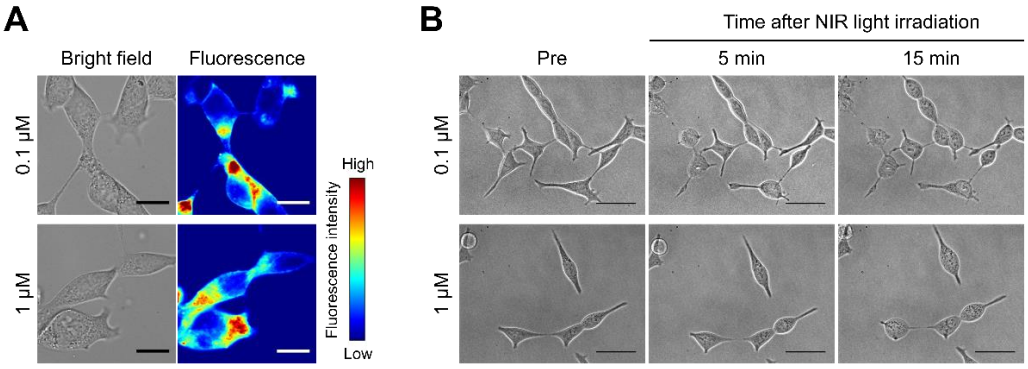

Figure S4. Microscopic observation of cells incubated with LMW-IR700 at different concentration (final concentration of IR700: 0.1 or 1 μM) for 1 h at 37°C. (A) IR700 fluorescence observed by fluorescence microscopy. There was no significant difference in fluorescence intensity and subcellular localization of IR700. Scale bar: 20 μm. (B) Morphological changes before and after light exposure. Plasma membrane damage were not influenced by the concentration of LMW-IR700 in the medium. Scale bar: 50 μm.